Hierarchical NH_2-MIL-88B(Fe)-derived Fe_3O_4@porous carbon/g-C_3N_4 nanocomposite for magnetically recoverable visible light photocatalysis of azo dyes

Martin Osemba[1]*, Loice Ojwang[2], Adrián Chávez Huerta[3], Samuel Karenga[1], Godffrey Keru[4]

[1] *Department of Natural Sciences, Mount Kenya University, Thika 342-01000, Kenya*

[2] *Department of Mathematics, Statistics and Physical Sciences, School of Science and Informatics, Taita Taveta University, Voi 635-80300, Kenya*

[3] *Research and Development Division, Zulian Institute of Technological Research Foundation, La Cañada de Urdaneta, Zulia 4033, Venezuela*

[4] *Department of Chemistry, Whitworth University, 300 W. Hawthorne Road, Spokane, WA 99251, USA*

**Authors to whom correspondence should be addressed:*

[1]*Department of Natural Sciences*
Mount Kenya University, Thika 342-01000
Kenya

Email: mouma@associates.mku.ac.ke
ORCID ID: https://orcid.org/0009-0007-2045-4746

This article has been accepted for publication and undergone full peer review but has not been through the copyediting, typesetting, and proofreading process, which may lead to differences between this version and the official version of record.

Please cite this article as: Osemba M., Ojwang L., Huerta A.C., Karenga S., Keru G. Hierarchical NH_2-MIL-88B(Fe)-derived Fe_3O_4@porous carbon/g-C_3N_4 nanocomposite for magnetically recoverable visible light photocatalysis of azo dyes. *Mongolian Journal of Chemistry*, 27(56), 2026, xx-xx

https://doi.org/10.5564/mjc.v27i56.5389

Hierarchical NH_2-MIL-88B(Fe)-derived Fe_3O_4@porous carbon/g-C_3N_4 nanocomposite for magnetically recoverable visible light photocatalysis of azo dyes

Martin Osemba[1]*, https://orcid.org/0009-0007-2045-4746
Loice Ojwang[2], https://orcid.org/0000-0001-8339-6618
Adrián Chávez Huerta[3], https://orcid.org/0000-0002-5094-4478
Samuel Karenga[1], https://orcid.org/0009-0008-1562-383X
Godffrey Keru[4], https://orcid.org/0000-0002-4879-2196

[1] Department of Natural Sciences, Mount Kenya University, Thika 342-01000, Kenya
[2] Department of Mathematics, Statistics and Physical Sciences, School of Science and Informatics, Taita Taveta University, Voi 635-80300, Kenya
[3] Research and Development Division, Zulian Institute of Technological Research Foundation, La Cañada de Urdaneta, Zulia 4033, Venezuela
[4] Department of Chemistry, Whitworth University, 300 W. Hawthorne Road, Spokane, WA 99251, USA

ABSTRACT

A hierarchical Fe_3O_4@porous carbon/g-C_3N_4 nanocomposite was synthesized from NH_2-MIL-88B(Fe) through controlled pyrolysis and heterojunction assembly for visible-light photocatalytic degradation of azo dyes. Structural and optical characterization confirmed the formation of a porous heterostructure with enhanced visible-light absorption and charge separation. Under visible-light irradiation ($\lambda > 420$ nm), the composite achieved degradation efficiencies of 98.6% for methyl orange and 96.8% for Congo red within 90 min. The catalyst exhibited a saturation magnetization of 32.4 emu g^{-1}, enabling rapid magnetic separation within approximately 20 s. Radical trapping experiments indicated that •OH and $•O_2^-$ were the dominant reactive species, supporting a Z-scheme charge-transfer mechanism. The nanocomposite retained 92.3% of its initial photocatalytic efficiency after five cycles, demonstrating good stability, reusability, and potential for sustainable wastewater treatment.

Keywords: *NH_2-MIL-88B(Fe); Fe_3O_4@porous carbon; g-C_3N_4; photocatalysis; azo dyes; magnetic recovery; Z-scheme heterojunction*

INTRODUCTION

The increasing discharge of synthetic dyes from textile, printing, leather, pharmaceutical, and related industries has become a significant environmental concern because of their persistence, intense coloration, and potential adverse effects on aquatic ecosystems. Azo dyes constitute one of the largest classes of synthetic colorants and are characterized by one or more azo (–N=N–) groups that contribute to their chemical stability and resistance to conventional biological treatment [1, 2, 3]. Representative compounds such as methyl orange (MO) and Congo red (CR) can persist in wastewater and reduce light penetration in receiving water bodies, thereby interfering with photosynthetic processes and aquatic productivity. Their complex aromatic structures also make complete mineralization difficult using conventional treatment methods. Consequently, the development of efficient and environmentally sustainable technologies for the removal and degradation of azo dyes remains an important research objective [4, 5].

Heterogeneous photocatalysis has attracted considerable attention as an advanced treatment technology because it can utilize light energy to generate highly reactive charge carriers and reactive oxygen species capable of transforming persistent organic contaminants into less harmful products. Semiconductor photocatalysts such as TiO_2 and ZnO have demonstrated high photocatalytic activity; however, their relatively wide band gaps restrict their utilization primarily to ultraviolet irradiation [6, 7]. Graphitic carbon nitride (g-C_3N_4), a metal-free semiconductor with a band gap of approximately 2.7 eV, has therefore emerged as a promising visible-light-responsive photocatalyst. Its chemical stability, suitable electronic structure, and relatively simple preparation have stimulated extensive investigation for environmental photocatalysis. Nevertheless, pristine g-C_3N_4 commonly suffers from rapid electron–hole recombination, limited surface area, and insufficient utilization of visible light, which can reduce its photocatalytic efficiency. These limitations have motivated the development of g-C_3N_4-based heterostructures and composites that improve charge separation, light harvesting, and surface accessibility [8, 9].

Metal–organic frameworks (MOFs) provide an attractive platform for constructing advanced photocatalytic materials because of their tunable structures, high porosity, and ability to serve as precursors for functional carbonaceous materials. In particular, NH_2-MIL-88B(Fe), an iron-containing amino-functionalized MOF, possesses a well-defined framework and can undergo controlled thermal transformation to produce iron oxide/carbon architectures. MOF-derived materials can retain aspects of the precursor's porous structure while generating new physicochemical properties associated with carbonization and metal-oxide formation.

Such transformations provide opportunities to construct hierarchical materials with interconnected pores, high surface areas, and improved accessibility of active sites [10, 11]. Combining MOF-derived Fe_3O_4@porous carbon with g-C_3N_4 is therefore potentially advantageous because the resulting material can integrate visible-light photocatalytic activity with the structural and electronic benefits of a porous carbon/iron oxide component [12].

Recent studies have demonstrated that coupling g-C_3N_4 with other semiconductors, carbon materials, and MOF-derived structures can enhance photocatalytic performance by promoting interfacial charge transfer and suppressing electron–hole recombination. Z-scheme heterojunctions are particularly attractive because they can preserve strongly reducing electrons and strongly oxidizing holes while improving charge separation [13, 14, 15]. In addition, incorporation of magnetic Fe_3O_4 offers an important practical advantage for water-treatment applications. Following photocatalytic treatment, magnetic composites can be rapidly separated from aqueous media using an external magnetic field, potentially reducing catalyst loss and simplifying recycling [16, 17, 18, 19]. Despite these advances, achieving an appropriate combination of hierarchical porosity, efficient visible-light harvesting, effective interfacial charge separation, magnetic recoverability, and long-term stability within a single photocatalyst remains challenging. Existing g-C_3N_4-based and MOF-derived photocatalysts frequently address only some of these requirements, while simultaneous integration of these characteristics has received comparatively limited attention. In particular, magnetically recoverable Z-scheme photocatalysts derived from NH_2-MIL-88B(Fe) remain insufficiently explored [20, 21, 22].

Accordingly, the present study reports the fabrication of a hierarchical Fe_3O_4@porous carbon/g-C_3N_4 nanocomposite derived from NH_2-MIL-88B(Fe) for visible-light photocatalytic degradation of azo dyes. The material was prepared through controlled pyrolysis of NH_2-MIL-88B(Fe) to generate Fe_3O_4@porous carbon, followed by assembly with exfoliated g-C_3N_4. The resulting heterostructure was systematically characterized to establish its structural, morphological, textural, optical, electronic, and magnetic properties. Its photocatalytic activity was evaluated using methyl orange and Congo red as representative azo dyes under visible-light irradiation. Particular attention was given to the relationship between hierarchical porosity, visible-light absorption, interfacial charge transfer, and photocatalytic performance. Radical-trapping experiments were further employed to identify the principal reactive species and to clarify the proposed photocatalytic mechanism. Finally,

the magnetic separation capability and photocatalytic recyclability of the nanocomposite were investigated to assess its practical potential for sustainable wastewater treatment.

EXPERIMENTAL

Materials

Ferric chloride hexahydrate ($FeCl_3 \cdot 6H_2O$, 99%, Sigma-Aldrich, USA), 2-aminoterephthalic acid (NH_2-BDC, 99%, Sigma-Aldrich, USA), N, N-dimethylformamide (DMF, 99.8%, Merck, Germany), methanol (99%, Merck, Germany), melamine (99%, Sigma-Aldrich, USA), methyl orange, and Congo red (Sigma-Aldrich) were used as received without further purification.

Synthesis of NH_2-MIL-88B(Fe)

A solution containing 10.0 mmol of $FeCl_3 \cdot 6H_2O$ and 10.0 mmol of NH_2-BDC by dissolving 2.70 g and 1.81 g in 60 mL of DMF under stirring for 30 minutes respectively. The homogeneous solution was transferred into a 100 mL Teflon lined autoclave and heated at 150 °C for 12 hours. The solvothermal synthesis yielded 2.35 g of NH_2-MIL-88B(Fe) from the three batches. After cooling to a room temperature, the resulting orange precipitate was collected by centrifugation at 8000 rpm for 10 minutes, washed three times with 30 mL DMF and 30 mL methanol, and dried at 80 °C for 12 hours.

Preparation of Fe_3O_4@Porous Carbon

2.00 g of the dried NH_2MIL88B(Fe) material was placed in a tubular furnace and heated to 500 °C at a heating rate of 5 °C min^{-1} under a nitrogen flow of 100 mL min^{-1}. The temperature was maintained at 500 °C for 3 hours. The obtained black powder was cooled naturally to room temperature and denoted as Fe_3O_4@PC.

Synthesis of g-C_3N_4

10.0 g of melamine was placed in a covered alumina crucible and heated at 550 °C for 4 hours with a ramp rate of 3 °C min^{-1} in air. The resulting yellow product was ground into powder. Exfoliation was achieved by ultrasonication in 200 mL ethanol for 2 hours, followed by drying at 60 °C.

Fabrication of Fe_3O_4@PC/g-C_3N_4 Nanocomposite

A mixture of 0.50 g of Fe_3O_4@PC and 1.00 g of g-C_3N_4 was dispersed in 150 mL ethanol and ultrasonicated for 1 hour. The suspension was stirred at 500 rpm for 12 hours at room temperature, followed by solvent evaporation at 60 °C. The dried composite was further annealed at 300 °C for 2 hours under nitrogen.

Diagrammatic Scheme of Synthesis

The overall synthesis strategy for the hierarchical Fe_3O_4@porous carbon/g-C_3N_4 nanocomposite is schematically illustrated in Figure 1**.** First, NH_2-MIL-88B(Fe) was prepared through a solvothermal reaction of $FeCl_3 \cdot 6H_2O$ and 2-aminoterephthalic acid (NH_2-BDC) in DMF at 150 °C for 12 h. The resulting MOF precursor was subsequently subjected to controlled pyrolysis at 500 °C under a continuous nitrogen atmosphere, during which the organic framework was carbonized and the iron-containing nodes were transformed into Fe_3O_4 nanoparticles embedded within the resulting porous carbon matrix, producing Fe_3O_4@PC. Finally, the Fe_3O_4@PC material was combined with exfoliated g-C_3N_4 through ultrasonication-assisted self-assembly in ethanol, followed by drying and mild annealing under nitrogen to promote intimate interfacial contact between the two components. As summarized in Figure 1, this sequential MOF formation–pyrolysis–heterostructure assembly approach was designed to integrate the hierarchical porous structure and magnetic functionality of Fe_3O_4@PC with the visible-light-responsive photocatalytic properties of g-C_3N_4, yielding the targeted Fe_3O_4@PC/g-C_3N_4 nanocomposite.

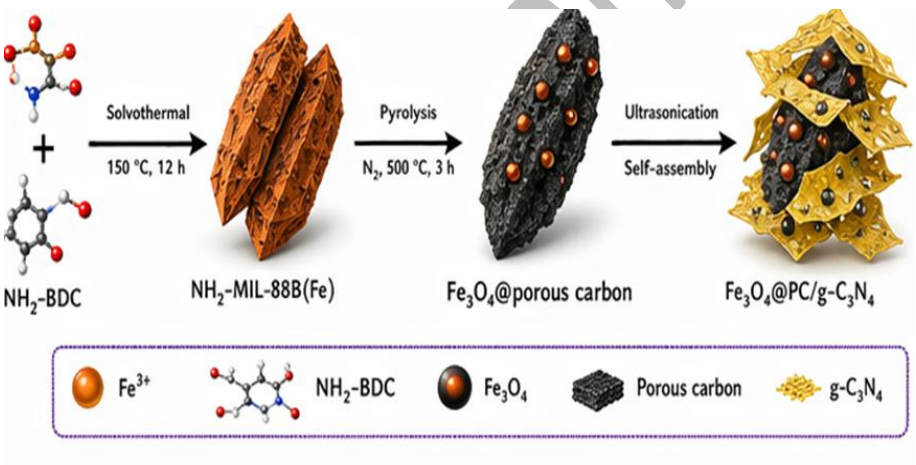

Fig. 1. Schematic illustration of the synthesis route for the hierarchical Fe_3O_4@porous carbon/g-C_3N_4 nanocomposite derived from NH_2-MIL-88B(Fe), showing MOF formation, pyrolysis-induced carbonization and Fe_3O_4 formation, exfoliation of g-C_3N_4, and subsequent heterojunction assembly.

Photocatalytic activity evaluation and reproducibility

All photocatalytic degradation experiments were conducted in triplicate under identical experimental conditions. The reported degradation efficiencies represent the average values of three independent measurements. The relative standard deviation (RSD) was below 5%, confirming good reproducibility and experimental reliability.

Characterization techniques

The structural properties of the synthesized materials were investigated using X-ray diffraction (XRD, Bruker D8 Advance) analysis performed with Cu Kα radiation (λ = 1.5406 Å) over a 2θ range of 5–80°, enabling phase identification and crystallinity assessment. The morphological features and surface architecture of the samples were examined using scanning electron microscopy (SEM, JEOL JSM-7600F), while detailed microstructural information and particle dispersion were further analyzed by transmission electron microscopy (TEM, JEOL JEM-2100). The chemical bonding and functional groups present in the materials were identified using Fourier transform infrared (FTIR) spectroscopy, recorded using a Thermo Scientific Nicolet iS10 spectrometer in the range of 400–4000 cm^{-1}. Surface elemental composition and oxidation states were determined through X-ray photoelectron spectroscopy (XPS, Thermo Scientific K-Alpha), providing insights into the chemical environment and interfacial interactions within the composite. Optical properties, including light absorption behavior were obtained using a Shimadzu UV-2600 spectrophotometer equipped with an integrating sphere using $BaSO_4$ as a reference, where UV–Vis diffuse reflectance spectroscopy (DRS), and the corresponding band gap energies were estimated using the Tauc method. Photoluminescence (PL) spectra were recorded at room temperature with an excitation wavelength of 325 nm, this was employed to investigate the recombination behavior of photogenerated electron–hole pairs, thereby assessing charge separation efficiency. The magnetic properties of the Fe_3O_4 containing composite were analyzed using vibrating sample magnetometry (VSM, Lakeshore 7404) at room temperature to determine the saturation magnetization and magnetic recoverability. Additionally, the specific surface area, pore size distribution, and pore volume of the materials were measured using Brunauer–Emmett–Teller (BET, Micromeritics ASAP 2020 analyzer) nitrogen adsorption–desorption analysis, providing information on the porous structure and its role in facilitating mass transfer during photocatalytic reactions.

RESULTS AND DISCUSSION

Structural and Morphological Analysis

The crystalline structure and phase transformation of the synthesized materials were systematically investigated using XRD, as presented in Figure 2. The diffraction pattern of the pristine NH_2 MIL88B(Fe) precursor exhibits a well-defined peak consistent with its crystalline framework, confirming the successful formation of the MOF structure. After pyrolysis at 500 °C under a nitrogen atmosphere, these characteristic peaks disappear and are replaced by new diffraction peaks at 2θ values of approximately 30.2°, 35.5°, 43.3°,

53.5°, 57.1°, and 62.6°, which can be indexed to the (220), (311), (400), (422), (511), and (440) crystal planes of cubic Fe_3O_4 (JCPDS No. 19-0629). This clearly demonstrates the successful conversion of NH_2 MIL 88B(Fe) into crystalline Fe_3O_4 nanoparticles.

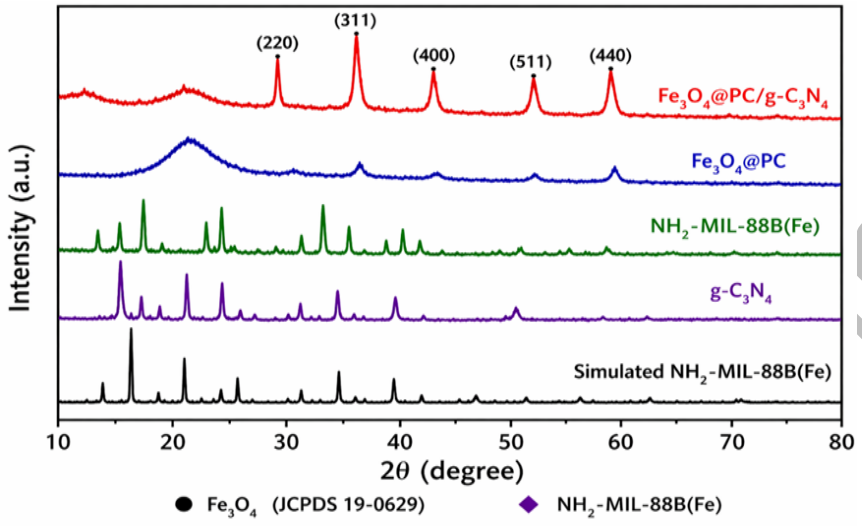

Fig. 2. X-ray diffraction (XRD) patterns of NH_2-MIL-88B(Fe), Fe_3O_4@porous carbon, and Fe_3O_4@PC/g-C_3N_4 nanocomposite confirming phase transformation and successful composite formation.

In addition, a broad diffraction peak centered at approximately 26.5° is observed in the Fe_3O_4@PC/gC_3N_4 composite, corresponding to the (002) plane of graphitic carbon and gC_3N_4. The broad nature of this peak suggests partial graphitization and structural disorder, which is advantageous for enhancing charge mobility and electron transport. The absence of any impurity peaks further confirms the high purity and successful integration of Fe_3O_4@porous carbon with g-C_3N_4. Similar phase evolution from Fe-based MOFs into crystalline Fe_3O_4/carbon composites has been reported previously for MOF-derived photocatalysts and environmental catalysts [23-27].

The morphological features of the materials were examined using SEM, as shown in Figure 3. The NH_2MIL88B(Fe) precursor exhibits an elaborate spindle like morphology with smooth surfaces. After pyrolysis, this morphology is largely retained, confirming the templating effect of the MOF precursor. However, the surface becomes significantly rougher and develops numerous pores due to decomposition of the organic ligands and evolution of volatile species during carbonization. The resulting hierarchical porous structure increases the accessible surface area and provides abundant active sites for photocatalytic reactions. After coupling with g-C_3N_4, thin nanosheets are observed surrounding the Fe_3O_4@porous carbon particles, indicating successful heterojunction formation. Such hierarchical porous

architectures have been shown to enhance reactant diffusion and increase photocatalytic active-site accessibility [28-33].

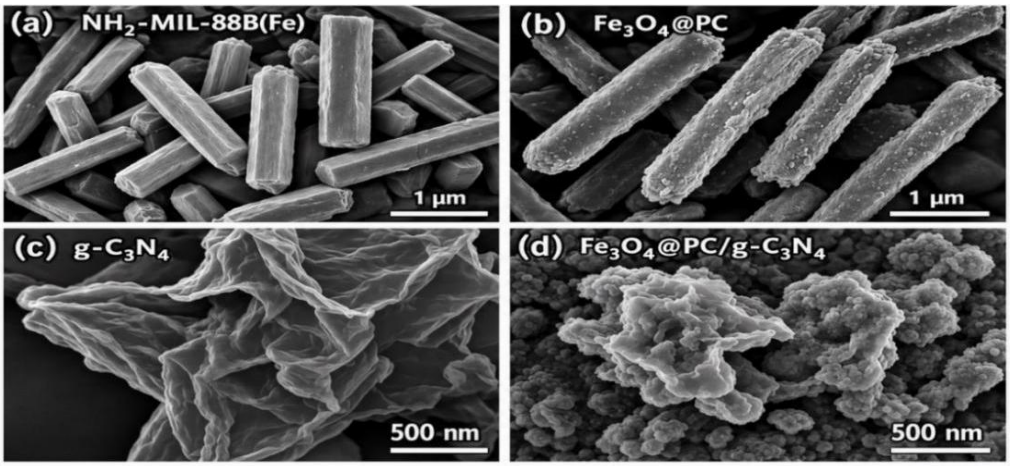

Fig. 3. Scanning electron microscopy images illustrating the morphological evolution from NH_2 MIL88B(Fe) precursor to Fe_3O_4@porous carbon and the assembled Fe_3O_4@PC/gC_3N_4 composite.

Further insights into the microstructure were obtained from transmission electron microscopy (TEM), as depicted in Figure 4. The images reveal that Fe_3O_4 nanoparticles with an average size of approximately 12.5 nm are uniformly dispersed within the porous carbon matrix. The nanoparticles are well confined, preventing aggregation and ensuring high catalytic activity. Moreover, the intimate contact between Fe_3O_4@PC and the layered gC_3N_4 nanosheets is clearly observed, forming an elaborate heterojunction interface. The high-resolution TEM images show clear lattice fringes with an interplanar spacing of 0.253 nm, corresponding to the (311) plane of Fe_3O_4, confirming its crystalline nature. This strong interfacial coupling is crucial for facilitating efficient charge transfer and suppressing recombination.

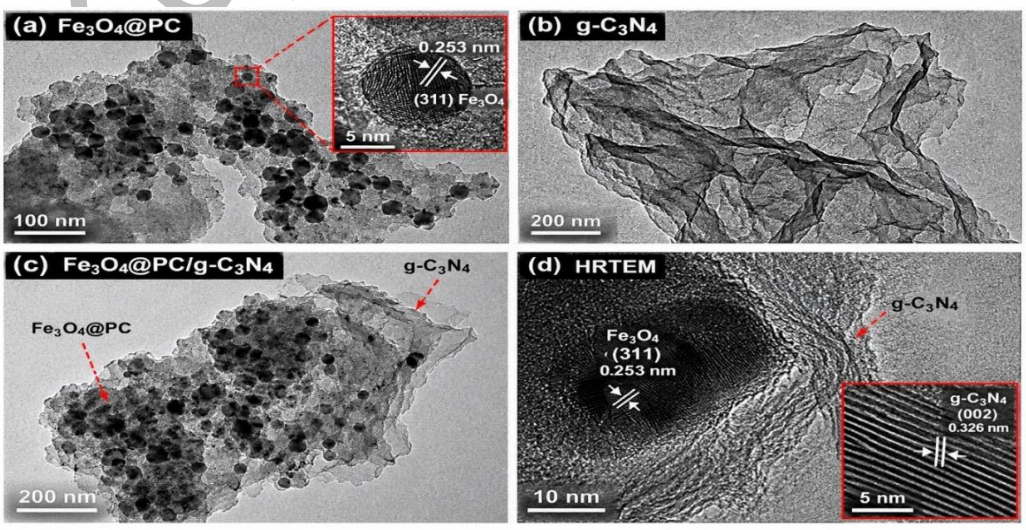

Fig. 4. TEM and HRTEM images of the Fe_3O_4@porous carbon/g-C_3N_4 nanocomposite: (a) Fe_3O_4@PC showing dispersed Fe_3O_4 nanoparticles within the porous carbon matrix; (b) exfoliated g-C_3N_4 nanosheets; (c) Fe_3O_4@PC/g-C_3N_4 heterostructure showing intimate interfacial contact; and (d) HRTEM image of the Fe_3O_4@PC/g-C_3N_4 interface.

Surface area and porosity

The nitrogen adsorption desorption isotherms and pore size distribution of the Fe_3O_4@PC/gC_3N_4 composite are presented in Figure 5. The isotherm exhibits a typical type IV curve with a pronounced hysteresis loop, indicating the presence of mesoporous structures. The Brunauer Emmett teller (BET) surface area is calculated to be 182.6 $m^2\ g^{-1}$, which is significantly higher than that of bulk gC_3N_4, reflecting the contribution of the MOF derived porous carbon. The high surface area is consistent with previous reports on MOF-derived porous carbon photocatalysts where hierarchical porosity significantly improved adsorption and photocatalytic performance [34-37].

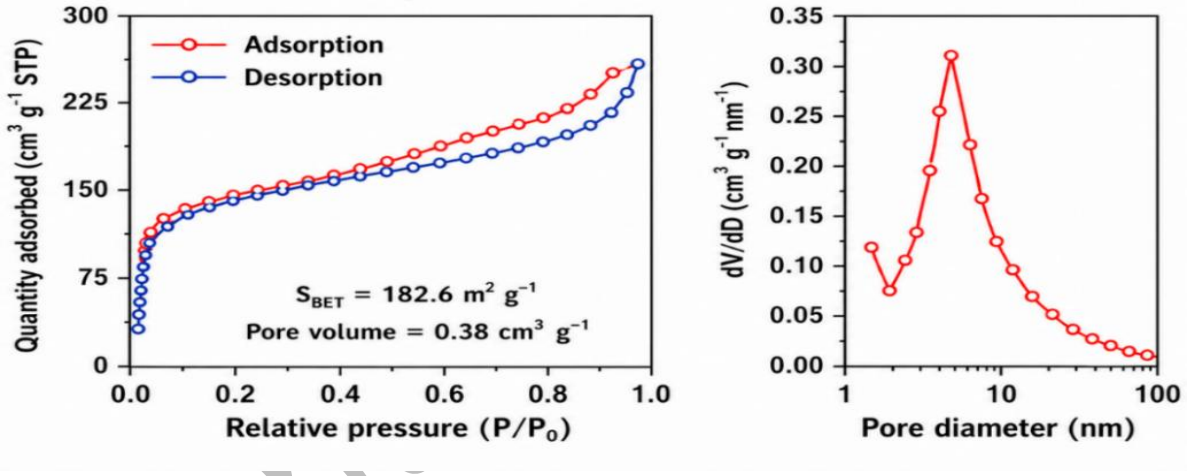

Fig. 5. Nitrogen adsorption–desorption isotherms and corresponding pore size distribution of Fe_3O_4@PC/g-C_3N_4 nanocomposite, demonstrating hierarchical mesoporous structure and high surface area.

The pore size distribution curve reveals a hierarchical porous structure consisting of mesopores of between 2–20 nm and macropores. This hierarchical architecture plays a vital role in photocatalysis by facilitating efficient mass transfer of dye molecules and reaction intermediates. The large surface area enhances adsorption capacity, while the interconnected pore network allows rapid diffusion, minimizing mass transfer limitations. These characteristics collectively contribute to the improved photocatalytic performance of the composite.

Optical properties

The optical absorption properties of the samples were analyzed using UV–Vis diffuse reflectance spectroscopy (DRS), as shown in figure 6 (a). Pristine gC_3N_4 exhibits an absorption edge around 460 nm, corresponding to a band gap of approximately 2.7 eV. In contrast, the Fe_3O_4@PC/gC_3N_4 composite displays a significantly extended absorption edge of up to 650 nm, indicating enhanced visible light absorption. Similar red-shifted absorption behavior has been observed in g-C_3N_4-based heterojunction photocatalysts due to enhanced electronic coupling and improved visible-light harvesting [38-43].

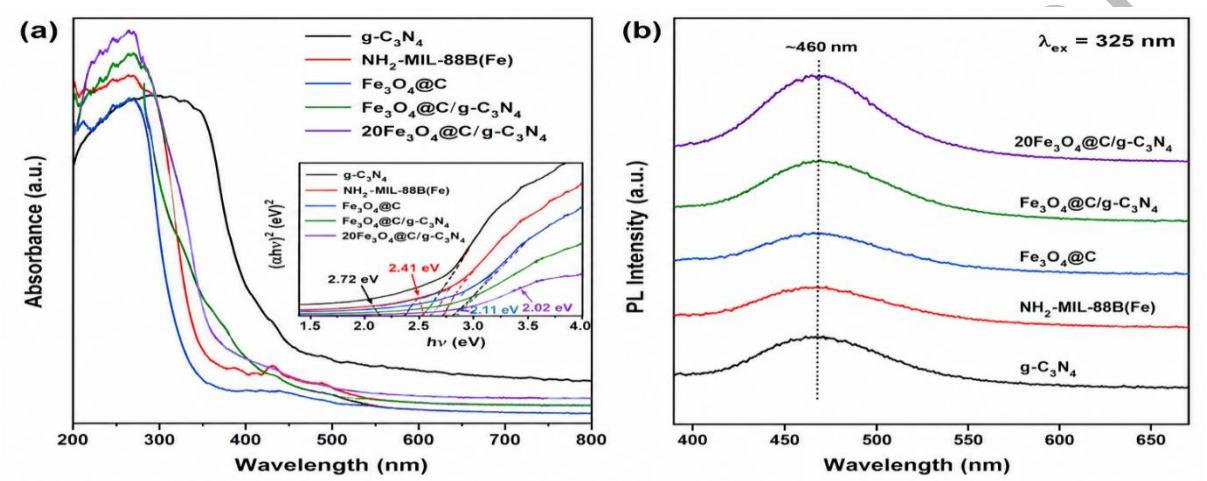

Fig. 6. (a) UV–Vis diffuse reflectance spectra and Tauc plots of g-C_3N_4 and Fe_3O_4@PC/g-C_3N_4; (b) photoluminescence spectra (λ_{ex} = 325 nm) illustrating the suppressed electron–hole recombination in the Fe_3O_4@PC/g-C_3N_4 nanocomposite.

The optical band gap of the composite was estimated to be 2.35 eV using Tauc plot analysis, confirming improved light harvesting capability. This red shift can be attributed to the synergistic interaction between Fe_3O_4, porous carbon, and g-C_3N_4, which modifies the electronic structure and promotes visible light responsiveness. Photoluminescence (PL) spectra shown in figure 6 (b) provide insight into the recombination behavior of photogenerated electron–hole pairs. The composite exhibits a markedly lower emission intensity compared to pure g-C_3N_4. Reduced PL intensity is commonly associated with suppressed electron–hole recombination and improved charge separation efficiency in heterostructured photocatalysts [44-50]. This improvement is attributed to the formation of a heterojunction and the presence of conductive porous carbon, which facilitates electron transport and acts as a charge mediator. The reduced recombination rate directly correlates with enhanced photocatalytic activity.

Magnetic properties

The magnetic behavior of the Fe_3O_4@PC/g-C_3N_4 composite was evaluated using VSM, as illustrated in figure7. The VSM curve exhibits negligible coercivity (Hc ≈ 0 Oe) and remanent

magnetization (Mr ≈ 0 emu g^{-1}), indicating superparamagnetic behavior characteristic of nanoscale Fe_3O_4 particles. The saturation magnetization value of 32.4 emu g^{-1} is lower than bulk Fe_3O_4 due to the presence of nonmagnetic porous carbon and g-C_3N_4 components.

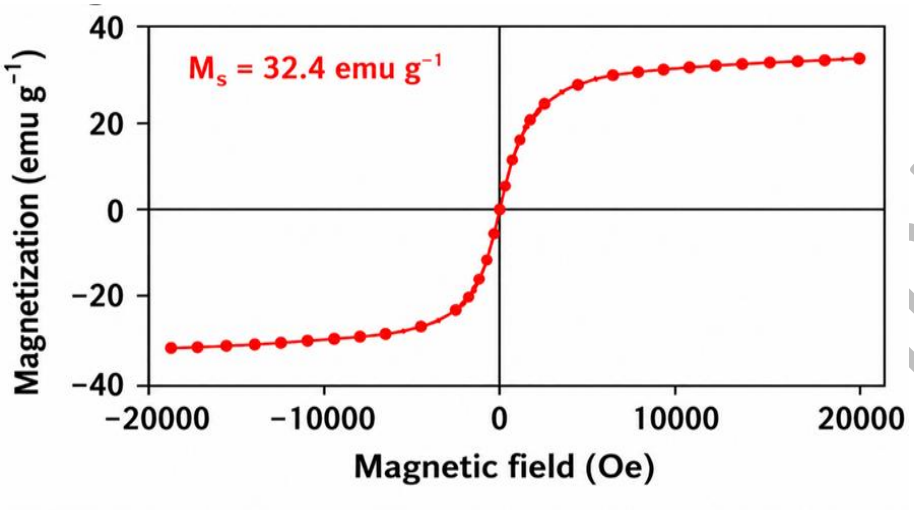

Fig. 7. Vibrating sample magnetometry (VSM) curve of Fe_3O_4@PC/g-C_3N_4 composite showing superparamagnetic behavior and high saturation magnetization for magnetic recovery.

Nevertheless, the saturation magnetization value of 32.4 emu g^{-1} compares favorably with previously reported magnetic g-C_3N_4-based photocatalysts, which typically exhibit saturation magnetization values between 18 and 30 emu g^{-1} after incorporation of nonmagnetic photocatalytic phases [51-54]. The near-zero coercivity and remanence indicate superparamagnetic behavior characteristic of nanosized Fe_3O_4 particles. The catalyst could be completely separated from aqueous suspension within approximately 20 s using an external magnet.

Photocatalytic performance

The photocatalytic activity of the Fe_3O_4@PC/g-C_3N_4 composite was evaluated through the degradation of methyl orange (MO) and Congo red (CR) under visible light irradiation, as shown in Figure 8 (a) and (b), respectively. Prior to irradiation, the suspensions were stirred in the dark to establish adsorption–desorption equilibrium.

As shown in figure 8a, the composite achieves a degradation efficiency of 98.6% for methyl orange within 90 minutes, while figure 8b shows a degradation efficiency of 96.8% for Congo red under identical conditions. In comparison, pure g-C_3N_4, Fe_3O_4@PC, and photolysis exhibit significantly lower degradation efficiencies, highlighting the superior performance of the heterostructured composite. The degradation kinetics follow a pseudo first order model, and the apparent rate constant (k) for methyl orange degradation is calculated to be 0.041 min^{-1}, which is approximately 3.2 times higher than that of pristine g-C_3N_4.

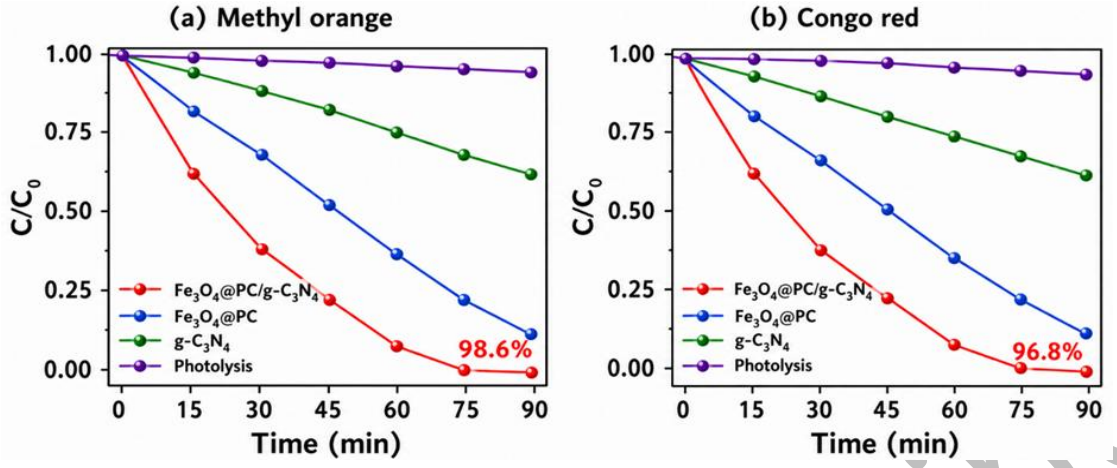

Fig. 8. Photocatalytic degradation performance under visible light irradiation: (a) methyl orange (MO) and (b) Congo red (CR) degradation profiles using Fe_3O_4@PC/g-C_3N_4 and control samples.

The enhanced photocatalytic activity can be attributed to several synergistic factors, including improved visible-light absorption, efficient charge separation via the heterojunction, enhanced electron transport through the porous carbon matrix, and increased active sites due to the hierarchical structure. Similar improvements have been reported for MOF/g-C_3N_4 and metal oxide/g-C_3N_4 heterostructures, where efficient charge separation and broadened visible-light absorption significantly enhanced degradation kinetics [55-59].

To further evaluate the effectiveness of the synthesized Fe_3O_4@PC/g-C_3N_4 nanocomposite, its photocatalytic performance was compared with recently reported visible-light-responsive photocatalysts for dye degradation. As summarized in Table 1, the present catalyst exhibits competitive degradation efficiency and shorter reaction time compared with several state-of-the-art photocatalytic systems reported in the literature. The superior performance can be attributed to the synergistic effects of the hierarchical porous structure, enhanced visible-light absorption, efficient Z-scheme charge separation, and rapid electron transport.

Table 1. Comparison of the photocatalytic performance of Fe_3O_4@PC/g-C_3N_4 with recently reported visible-light-responsive photocatalysts for dye degradation.

Photocatalyst	Pollutant	Degradation (%)	Time (min)	Reference
MOF-5/g-C_3N_4	Rhodamine B	92.4	120	Haris *et al*., 2024
MoS_2/g-C_3N_4	Aniline Green	95.0	120	Ramalingam *et al*., 2025
La/Cu-$BiFeO_3$/g-C_3N_4	Crystal Violet	96.2	100	Bibi *et al*., 2025
Ti_3C_2/g-C_3N_4 Hydrogel	Organic Pollutants	94.8	120	Li *et al*., 2025
Fe_3O_4@PC/g-C_3N_4	**Methyl Orange**	**98.6**	**90**	**This work**
Fe_3O_4@PC/g-C_3N_4	**Congo Red**	**96.8**	**90**	**This work**

The comparison demonstrates that the Fe_3O_4@PC/g-C_3N_4 nanocomposite achieves one of the highest degradation efficiencies among recently reported visible-light photocatalysts while maintaining the additional advantage of magnetic recoverability. The incorporation of MOF-derived porous carbon not only improves charge transport and visible-light harvesting but also enhances structural stability and facilitates catalyst recovery, making the material attractive for practical wastewater treatment applications.

Mechanism study

To identify the dominant reactive species involved in the photocatalytic process, radical trapping experiments were conducted, and the results are presented in Figure 9. The addition of isopropanol (IPA), a hydroxyl radical scavenger, significantly reduces the degradation efficiency, indicating the crucial role of •OH radicals. Similarly, the presence of benzoquinone (BQ), a superoxide radical scavenger, also leads to a marked decrease in degradation efficiency, confirming the involvement of $\bullet O_2^-$ radicals. In contrast, the addition of EDTA shows a relatively smaller effect, suggesting a lesser contribution of photogenerated holes.

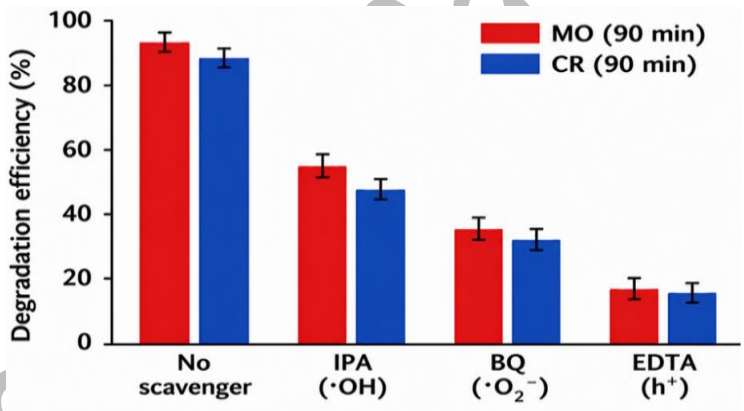

Fig. 9. Radical scavenging experiments identifying the dominant reactive species involved in photocatalytic degradation over Fe_3O_4@PC/g-C_3N_4 nanocomposite.

Based on these observations, a Z scheme charge transfer mechanism is proposed, as illustrated in figure 10. Under visible light irradiation, both g-C_3N_4 and Fe_3O_4@PC are photoexcited to generate electron–hole pairs. The photogenerated electrons in the conduction band of Fe_3O_4@PC recombine with holes in the valence band of g-C_3N_4 at the interface. This recombination pathway preserves the strong redox potentials of the remaining charge carriers.

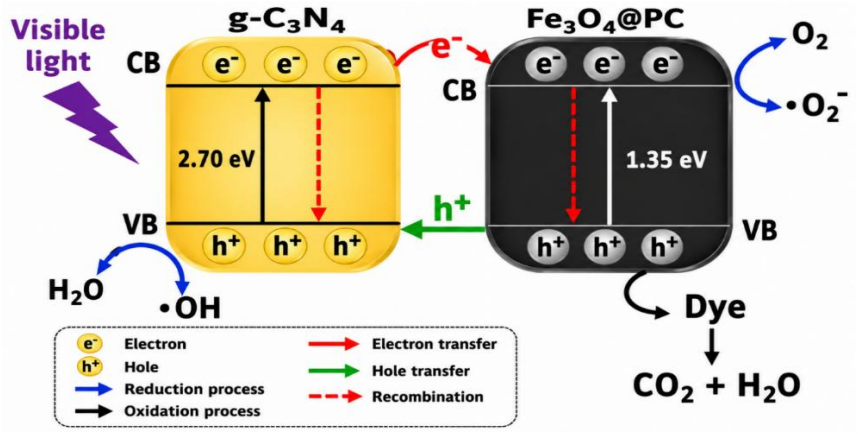

Fig. 10. Proposed Z-scheme charge transfer mechanism illustrating charge separation pathways and reactive oxygen species generation in the Fe_3O_4@PC/g-C_3N_4 heterojunction system.

As a result, electrons in the conduction band of g-C_3N_4 reduce molecular oxygen to form superoxide radicals (•O_2^-), while holes in the valence band of Fe_3O_4@PC oxidize water to generate hydroxyl radicals (•OH). These highly reactive species subsequently degrade dye molecules into CO_2 and H_2O. The Z-scheme mechanism effectively enhances charge separation while maintaining strong redox capabilities, leading to superior photocatalytic performance. Z-scheme heterojunction systems are widely recognized for preserving strong redox potentials while promoting efficient spatial separation of photogenerated charge carriers [60, 61, 62, 63].

Reusability and stability

The practical applicability of a photocatalyst in wastewater treatment critically depends on its stability and recyclability during repeated operation. To evaluate the durability of the Fe_3O_4@porous carbon/g-C_3N_4 nanocomposite, cyclic photocatalytic degradation experiments were carried out using methyl orange (MO) under visible light irradiation. After each cycle, the catalyst was magnetically separated from the reaction mixture, washed thoroughly with deionized water and ethanol to remove residual intermediates, and dried at 60 °C prior to reuse. As shown in figure 11, the Fe_3O_4@PC/g-C_3N_4 nanocomposite maintains a high photocatalytic activity over five successive cycles, retaining 92.3% of its initial degradation efficiency. Comparable long-term stability has been reported for advanced MOF-derived photocatalysts and adsorption-photocatalysis hybrid systems used in wastewater remediation [64, 65, 66, 67].

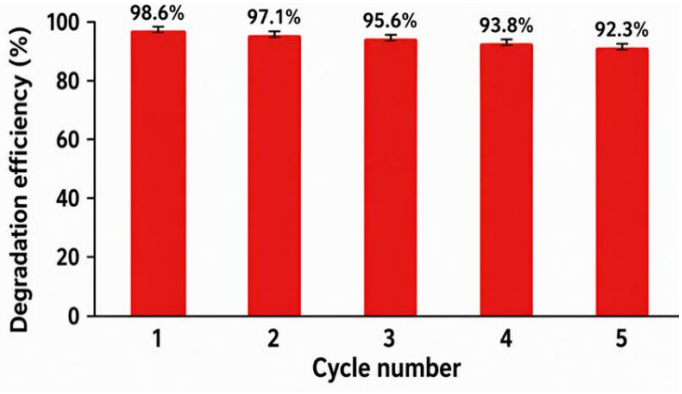

Fig. 11. Reusability and stability of Fe_3O_4@PC/g-C_3N_4 nanocomposite over five consecutive photocatalytic cycles.

The slight decline in performance of approximately 7.7% is attributed primarily to minor surface fouling caused by strongly adsorbed reaction intermediates and partial blockage of active sites, rather than any significant structural degradation of the catalyst. The excellent recyclability of the composite can be ascribed to its well-engineered structural features. The embedded Fe_3O_4 nanoparticles impart strong magnetic properties (M_s = 32.4 emu g^{-1}), enabling rapid and efficient recovery of the catalyst within seconds using an external magnetic field, thereby minimizing material loss. In addition, the porous carbon matrix derived from NH_2-MIL-88B(Fe) provides a robust structural framework that prevents nanoparticle aggregation and preserves the hierarchical porous architecture. Furthermore, the strong interfacial coupling between Fe_3O_4@porous carbon and g-C_3N_4 ensures the stability of the heterojunction, maintaining efficient charge separation and transfer during repeated photocatalytic cycles. The stability of the catalyst is further supported by the consistent magnetic separation behavior observed after each cycle, indicating that the Fe_3O_4 component remains firmly anchored within the carbon matrix without significant leaching. This structural robustness is essential for long-term operation and prevents secondary contamination of treated water. Overall, the results presented in figure 11 clearly demonstrate that the Fe_3O_4@PC/g-C_3N_4 nanocomposite possesses excellent reusability, structural stability, and operational convenience. These attributes highlight its strong potential for practical applications in sustainable wastewater treatment and large-scale photocatalytic processes.

CONCLUSION

A hierarchical Fe_3O_4@porous carbon/g-C_3N_4 nanocomposite derived from NH_2-MIL-88B(Fe) was successfully synthesized through MOF-templated pyrolysis and heterojunction assembly. The composite exhibited a high BET surface area of 182.6 m^2 g^{-1}, an extended

visible-light absorption edge reaching 650 nm, and a reduced bandgap energy of 2.35 eV. The photocatalyst achieved degradation efficiencies of 98.6% for methyl orange and 96.8% for Congo red within 90 min under visible-light irradiation. The saturation magnetization of 32.4 emu g^{-1} enabled rapid magnetic recovery within 20 s. Radical trapping experiments confirmed that •OH and $•O_2^-$ were the dominant reactive species and supported a Z-scheme charge transfer mechanism. The catalyst retained 92.3% of its initial activity after five consecutive cycles, demonstrating excellent stability and reusability. These results highlight the potential of MOF-derived magnetic heterojunction photocatalysts for sustainable wastewater treatment applications. The photocatalytic efficiency achieved in this work compares favorably with recently reported visible-light-responsive MOF/g-C_3N_4 heterojunction systems, while additionally providing rapid magnetic recovery and excellent cycling stability

Funding Information

This research received no specific grant from any funding agency in the public, commercial, or not-for-profit sectors.

Author Contributions

MO: Conceptualization, methodology, investigation, data curation, formal analysis, visualization, and writing original draft preparation; LO: methodology, investigation, data analysis, and writing review and editing; ACH: characterization, data analysis, and interpretation; SK: supervision, methodology, and writing review and editing; GK: supervision, validation, and writing review and editing;

All authors contributed to the interpretation of the results, critically reviewed the manuscript, and approved the final version for publication.

REFERENCES

1. Xu B., Yang H., Cai Y., Yang H., Li C. (2016) Preparation and photocatalytic property of spindle-like MIL-88B(Fe) nanoparticles. *Inorg. Chem. Commun.,* **67**, 29–31. https://doi.org/10.1016/j.inoche.2016.03.003
2. Behera P., Priyadarshini P., Panda J., Parida K. (2025) Recent advances in NH_2-MIL-88B(Fe)-based photocatalysts for environmental remediation: design strategies, mechanisms, and applications. *Chem. Asian J.,* **20**, e202500541. https://doi.org/10.1002/asia.202500541

3. Gao Q., Sheng Q., Zhang S., Tang Y. (2025) Recent trends on MIL-88(Fe) metal–organic frameworks: synthesis and applications in pollutant removal and detection. *RSC Adv.,* **15**, 26184–26200. https://doi.org/10.1039/D5RA03049H
4. Ahmed A.S., Waheed I.F. (2026) Preparation of CNFO@g-C_3N_4-K magnetic nanocomposite for dual photodegradation of methylene blue and carbon dioxide adsorption. *Surf. Interfaces,* **82**, 108524. https://doi.org/10.1016/j.surfin.2026.108524
5. Mousavi M., Habibi-Yangjeh A. (2016) Magnetically separable ternary g-C_3N_4/Fe_3O_4/BiOI nanocomposites: novel visible-light-driven photocatalysts based on graphitic carbon nitride. *J. Colloid Interface Sci.,* 465, 83–92. https://doi.org/10.1016/j.jcis.2015.11.057
6. Afshari M., Esfandian H., Shahavi M.H. (2026) Synthesis and investigation of the supercapacitor behavior of iron oxide/graphitic carbon nitride nanocomposite derived from Fe-MOF. *Sci. Rep.,* **16**, 113. https://doi.org/10.1038/s41598-025-28958-8
7. Zhang X., Chen S., Guo F., Jing Q., Huo P., et al. (2024) A novel method for synthesizing specific surface area-modulable g-C_3N_4 photocatalyst with maize-like structure. *Appl. Surf. Sci.,* **651**, 159224. https://doi.org/10.1016/j.apsusc.2023.159224
8. Zhao Y., Wan X.Y., Wan-Me Z.X., Wen H.Z., Zhang H.T., Xie Y.L. (2026) Construction of porous sheet-like g-C_3N_4/CdS hierarchical heterojunctions and their application in photocatalytic hydrogen production. *Appl. Mater. Today,* **49**, 103130. https://doi.org/10.1016/j.apmt.2026.103130
9. Aslam F., Aslam T., Alzahrani F.M., Sunny M.N.M., Mehdi M.M., et al. (2025) Photocatalytic degradation of ciprofloxacin antibiotics via cobalt-doped spinel ferrites nanocomposite: synthesis, characterization, and mechanistic insights. *Catal. Lett.,* **155**, 352. https://doi.org/10.1007/s10562-025-05194-3
10. Srivastava A.P., Pandey B.K. (2026) Electronic structure and band-edge engineering of Sc-doped g-C_3N_4: a first-principles study. *Discov. Chem.,* **3**, 234. https://doi.org/10.1007/s44371-026-00701-w
11. Farid J., Kadhimi H., Al-Jubouri A. (2026) Nanoarchitectonics of two-dimensional materials for photocatalysis: design strategies, mechanistic insights, and application pathways. *J. Inorg. Organomet. Polym. Mater.,* **36**, 4716-4750. https://doi.org/10.1007/s10904-025-04158-9
12. Fattah-alhosseini A., Sangarimotlagh Z., Karbasi M., Duygulu O., Dikici B., et al. (2026) Ti_3C_2-MXene quantum dot/Fe-MOF heterostructure with enhanced visible-light

photocatalytic performance. *Adv. Compos. Hybrid Mater.,* **9**, 78. https://doi.org/10.1007/s42114-026-01622-z

13. Lee J., Kim J. (2024) Heterostructured photocatalytic fabric composed of Ag_3PO_4 nanoparticle-decorated NH_2-MIL-88B(Co/Fe) crystalline wires for Rhodamine B adsorption and degradation. *ACS Appl. Nano Mater.,* **7**, 8362–8375. https://doi.org/10.1021/acsanm.4c01560
14. Kabtamu D.M., Wu Y.-N., Li F. (2020) Hierarchically porous metal–organic frameworks: synthesis strategies, structure(s), and emerging applications in decontamination. *J. Hazard. Mater.,* **397**, 122765. https://doi.org/10.1016/j.jhazmat.2020.122765
15. Ji Y., Pan Z., Ma T., Wang K., Zhao X., Jin Q. (2024) Hierarchical porous spindle-shaped MIL-88B@Fe_2O_3 with core–shell structure for conductometric trimethylamine detection. *Sens. Actuators B Chem.,* **417**, 136103. https://doi.org/10.1016/j.snb.2024.136103
16. Khanum R., Ali R.A.S., Rangaswamy H.R., Santhosh Kumar S.R., Prashantha A.G., Jagadisha A.S. (2023) Recent review on synthesis, spectral studies, versatile applications of azo dyes and its metal complexes. *Results in Chemistry,* **5**, 100890. https://doi.org/10.1016/j.rechem.2023.100890
17. Chowdhury A.P., Anantharaju K.S., Keshavamurthy K., Rokhum S.L. (2023) Recent advances in efficient photocatalytic degradation approaches for azo dyes. *Journal of Chemistry,* **2023**, 9780955. https://doi.org/10.1155/2023/9780955
18. Morsy M., Hassan S.S., Shaker H.M., Ismail K.M. (2025) Synthesis and characterization of MIL-88B(Fe) MOF for high-performance humidity sensing. *Sens. Actuators B Chem.,* **438**, 137806. https://doi.org/10.1016/j.snb.2025.137806
19. Mandal D., Bharti L., Anshu S., Chandra A. (2026) 2D graphitic carbon nitride-based impedance sensor for vitamin D_3 detection. *Sens. Actuators A Phys.,* **409**, 118097. https://doi.org/10.1016/j.sna.2026.118097
20. Kumar S., Kumar V., Pathak C.S., Mishra A., Bansal M.K., Baghel R.S. (2026) A comprehensive review on ZnO wide-bandgap semiconductors: materials engineering, properties, and emerging applications. Results in Materials, **30**, 100929. https://doi.org/10.1016/j.rinma.2026.100929
21. Ahmed M.A., Mahmoud S.A., Mohamed A.A. (2024) Unveiling the photocatalytic potential of graphitic carbon nitride (g-C_3N_4): a state-of-the-art review. *RSC Advances,* **14**, 25629–25662. https://doi.org/10.1039/D4RA04234D
22. Zhong T., Huang W., Yao Z., Long X., Qu W., et al. (2024) Engineering of graphitic carbon nitride (g-C_3N_4) based photocatalysts for atmospheric protection: modification strategies,

recent progress, and application challenges. *Small,* **20**, 2404696. https://doi.org/10.1002/smll.202404696

23. Yu J., Wang S., Xie M., Wu Q., Shu Q. (2026) Construction of a direct Z-scheme $Zn_3V_2O_8$/g-C_3N_4 heterojunction for highly efficient photocatalytic degradation of Rhodamine B. *Diamond Relat. Mater.,* **164**, 113515. https://doi.org/10.1016/j.diamond.2026.113515
24. Ikreedeegh R.R., Hossen M.A., Sherryna A., Tahir M. (2024) Recent advances on synthesis and photocatalytic applications of MOF-derived carbon materials: a review. *Coordination Chemistry Reviews,* **510**, 215834. https://doi.org/10.1016/j.ccr.2024.215834
25. Shahzadi S., Akhtar M., Arshad M., Ijaz M.H., Ashraf Janjua M.R.S. (2024) A review on synthesis of MOF-derived carbon composites: innovations in electrochemical, environmental and electrocatalytic technologies. *RSC Advances,* **14**, 27575–27607. https://doi.org/10.1039/D4RA05183A
26. Ghamarpoor R., Fallah A., Jamshidi M. (2024) A review of synthesis methods, modifications, and mechanisms of ZnO/TiO_2-based photocatalysts for photodegradation of contaminants. *ACS Omega,* **9**, 25457–25492. https://doi.org/10.1021/acsomega.3c08717
27. Akkol C., Saka E.T., Senocak A. (2026) The performance of phthalocyanine-based catalysts for photocatalytic degradation of chlorophenols. *Inorg. Chem. Commun.,* **188**, 116457. https://doi.org/10.1016/j.inoche.2026.116457
28. Liang Z., Dai J., Zhao M., Ma J., Zhang J., et al. (2026) Z-scheme g-C_3N_4/$BiVO_4$ photocatalysts via hydrothermal tuning: charge transfer mechanism and machine-learning optimization. *J. Taiwan Inst. Chem. Eng.,* **181**, 106514. https://doi.org/10.1016/j.jtice.2025.106514
29. Wang S., Ke Y., Jin F., Jin Z. (2025) Charge separation engineering via $CoAl_2O_4$/ZnCdS heterojunction and d-band center modulation for synergistically enhanced photocatalytic hydrogen evolution. *J. Mater. Chem.* A, **13**, 34585–34598. https://doi.org/10.1039/D5TA05584A
30. Yuan C., Yin H., Lv H., Zhang Y., Li J., et al. (2023) Defect- and donor-manipulated highly efficient electron–hole separation in a 3D nanoporous Schottky heterojunction. *JACS Au,* **3**, 3127–3140. https://doi.org/10.1021/jacsau.3c00482

31. Yaseen H.S., Liu R., Deng L., Hassan F.U., Jiang Y., et al. (2026) Enhanced charge regulation in a bimetallic CoFe-MOF/g-C_3N_4 hybrid for efficient hydrogen evolution. *J. Mater. Sci.,* **61**, 14028–14043. https://doi.org/10.1007/s10853-026-12683-2
32. Habib A., Sun Y., Shao G., Zhang P. (2026) Electrospun m-ZrO_2/Cyano-g-C_3N_4 nanofiber heterostructure for photocatalytic solar fuel production. *Solar RRL,* **10**, e202500931. https://doi.org/10.1002/solr.202500931
33. Zhang J., Wang X., Wang X., Li C. (2025) Heterophase junction effect on photogenerated charge separation in photocatalysis and photoelectrocatalysis. *Acc. Chem. Res.,* **58**, 787–798. https://doi.org/10.1021/acs.accounts.4c00582
34. Li B., Zhang X., Chen M., Huang X., Fang X., et al. (2025) Multichannel charge transfer mediated by polyoxometalate-loaded SnS_2-wrapped Te nanostructures for efficient photocatalytic CO_2 reduction. *Appl. Catal. B Environ. Energy,* **377**, 125509. https://doi.org/10.1016/j.apcatb.2025.125509
35. Sayed M., Zhang L., García H., Yu H., Yu J. (2026) S-scheme shapes heterojunction photocatalysis. *Acc. Chem. Res.,* **59**, 1138–1153. https://doi.org/10.1021/acs.accounts.5c00899
36. Lai Z., Ashwini M.A., Susanti D., Sagadevan S., Ninwong B., et al. (2026) Facile synthesis of g-C_3N_4/Fe_3O_4/PANI ternary nanocomposite for supercapacitor and photocatalytic applications. *Diamond Relat. Mater.,* **162**, 113277. https://doi.org/10.1016/j.diamond.2025.113277
37. Ahmad S., Shah S.A., Ahmed S. (2026) Interface engineering of Nd-$BiFeO_3$/g-C_3N_4 coupled with polypyrrole for synergistically enhanced visible-light photocatalytic activity and advanced supercapacitor behavior. *Inorg. Chem. Commun.,* **188**, 116846. https://doi.org/10.1016/j.inoche.2026.116846
38. Zadegan S.P.K., Hosseini S.A., Taghavi L., Yengejeh R.J. (2026) Optimization of photocatalytic ozonation process using g-C_3N_4/NH_2-MIL-125(Ti)/TiO_2 nanocomposite for the degradation of microplastics in aquatic environments. *Int. J. Environ. Res.,* **20**, 182. https://doi.org/10.1007/s41742-026-01134-0
39. Abolghasemi S., Nasiri A., Hashemi M., Rajabi S., Rahimi F. (2025) Magnetic nanocomposites: innovative adsorbents for antibiotics removal from aqueous environments a narrative review. *Applied Water Science,* **15**, 30. https://doi.org/10.1007/s13201-025-02360-1
40. Lai Z., Ashwini M.A., Sagadevan S., Susanti D., Johan M.R. (2026) Synergic combination of g-C_3N_4/V_2O_5/PANI ternary nanocomposite for energy and environmental applications.

J. Inorg. Organomet. Polym. Mater., **36**, 2406–2423. https://doi.org/10.1007/s10904-025-04038-2

41. Dhilshada V.N., Shilpa M., Chattopadhyaya M. (2026) g-C_3N_4/CoN_4 heterojunction as a sensor for detecting volatile organic compounds: a density functional study. *RSC Adv.,* **16**, 3192–3206. https://doi.org/10.1039/D5RA04202J
42. Martins M.G., de Menezes F.L., Freire T.M., Araújo R.N., de Paula Santos V., et al. (2025) Photocatalytic applications of cardanol-derived meso-metalloporphyrins-based g-C_3N_4 nanocomposites. *Catal. Lett.,* **155**, 81. https://doi.org/10.1007/s10562-024-04916-3
43. Soni H., Kanjariya P., Ballal S., Panigrahi R., Ariffin I.A., Tantawi D., Abosaoda M.K., Nathiya D., Jayabalan K., Chauhan A.S. (2025) Recent advances in the synthesis of magnetic nanocomposites for the adsorption of heavy metal ions from wastewater. *J. Mol. Str.,* **1345**, 143019. https://doi.org/10.1016/j.molstruc.2025.143019
44. Shaalan N.M., Ahmad M.M., Alshehab A., Altayar A.R., Hamad D. (2026) Tailoring graphitic carbon nitride with sodium tin oxide for high-performance supercapacitors. *Int. J. Miner. Metall. Mater.* https://doi.org/10.1007/s12613-026-3374-0
45. Bhattacharjee J., Datta P., Shaikh A.A., Sathianarayanan A., Mandal M.K., Roy S. (2026) Photoelectrochemical hydrogen generation from seawater using modified g-C_3N_4/NiO photo-electrode heterojunction. *J. Appl. Mater. Sci.,* **2**, e260103. https://doi.org/10.22034/jams.2026.260103
46. Chen J., Guan X., Zhao D., Wang B., Shen S. (2026) Advancing photocatalytic overall water splitting with Z-scheme heterojunctions by interfacial manipulation. *Adv. Mater.,* **38**, e202515717. https://doi.org/10.1002/adma.202515717
47. Molaei M.J. (2024) Principles, mechanism, and identification of S-scheme heterojunction for photocatalysis: a critical review. *J. Am. Ceram. Soc.,* **107**, 5695–5719. https://doi.org/10.1111/jace.19920
48. Wang S., Hao W., Liu Z., Niu X., Wang L., Zhao Q. (2026) Two-dimensional direct Z-scheme heterojunction photocatalysts for highly efficient energy conversion and chemical synthesis. *ACS Nano,* **20**, 137–162. https://doi.org/10.1021/acsnano.5c18705
49. Malefane M.E., Mafa P.J., Managa M., Nkambule T.T.I., Kuvarega A.T. (2023) Understanding the principles and applications of dual Z-scheme heterojunctions: how far can we go? *J. Phys. Chem. Lett.,* **14**, 1029–1045. https://doi.org/10.1021/acs.jpclett.2c03387

50. Thakur S., Bharti S. (2025) Recent progress in metal–organic frameworks-based nanocomposites for antibiotic removal from water: an in-depth review. *Environ. Sci. Pollut. Res.,* **33**, 5211–5241. https://doi.org/10.1007/s11356-025-36155-3
51. Gaber M.M., Toghan A., Eldesoky A.M., Al-Hussain S.A., Masoud E.M., et al. (2025) Sustainable photocatalytic treatment of real pharmaceutical wastewater using a novel ZnO/MIP-202(Zr) bio-MOF hybrid synthesized via a green approach. *Catalysts,* **15**, 1017. https://doi.org/10.3390/catal15111017
52. Nabwey H.A., Tony M.A. (2026) Reimagining textile effluent treatment using metal–organic framework-based hybrid catalysts: a critical review. *Catalysts,* **16**, 355. https://doi.org/10.3390/catal16040355
53. Fattah-alhosseini A., Chaharmahali R., Nasiriani T., Veisi P., Dikici B., et al. (2026) Recent advances in photocatalytic membranes modified by quantum dots-based heterostructures: a comprehensive review. *Adv. Compos. Hybrid Mater.,* **9**, 111. https://doi.org/10.1007/s42114-026-01624-x
54. Samy M.S., Abou El Nadar H.M., Gomaa E.A., Ibrahim A.A., Adly M.S. (2026) Valorization of domestic wastes into Cu-MOF-derived CuO@ZnO nanocomposites for sustainable photocatalytic degradation of methylene blue and rhodamine B dyes. *Sci. Rep.,* **16**, 15042. https://doi.org/10.1038/s41598-026-51864-6
55. Asiri M., Sead F.F., Mayani S.V., Menon S.V., Thakur R., et al. (2025) Enhanced photocatalytic degradation of penicillin G using magnetic silica doped ZnAl-layered double hydroxides. *Sci. Rep.,* **15**, 33110. https://doi.org/10.1038/s41598-025-17327-0
56. Pervaiz S., Javed M., Shah A., Latif A., Nasir S., Shah I. (2025) Environmental applications of magnetic nanohybrid materials. *RSC Adv.,* **15**, 19899–19936. https://doi.org/10.1039/D5RA03470A
57. Zhao Y., Liu Y., Xu H., Fan Q., Zhu C., et al. (2023) Preparation and application of magnetic composites using controllable assembly for use in water treatment: a review. *Molecules,* **28**, 5799. https://doi.org/10.3390/molecules28155799
58. Liu M., Ye Y., Ye J., Gao T., Wang D., et al. (2023) Recent advances of magnetite (Fe_3O_4)-based magnetic materials in catalytic applications. *Magnetochemistry,* **9**, 110. https://doi.org/10.3390/magnetochemistry9040110
59. Sharshir S.W., Ataya S., El-Attar H.G., Lotfy L.A., Sowayan A., Khan R., Abdelfatah M., El-Shaer A. (2025) Nanocomposites for water treatment, photocatalysis, and challenges: a systematic review. *Global Challenges,* **9**, e00217. https://doi.org/10.1002/gch2.202500217

60. Li C., Lu H., Ding G., Li Q., Liao G. (2023) Recent advances on g-C_3N_4-based Z-scheme photocatalysts for organic pollutant removal. *Catalysis Science & Technology,* **13**, 2877–2898. https://doi.org/10.1039/D3CY00242J
61. Molaei M.J. (2026) Z-scheme heterojunction photocatalysts: principles, engineering strategies, and applications in solar-driven energy conversion and environmental remediation. *J. Chinese Chem. Soc.* **73**, (8) 1114–1131 https://doi.org/10.1002/jccs.70246
62. Luo Y., Zhu Y., Han Y., Ye H., Liu R., et al. (2023) g-C_3N_4-based photocatalysts for organic pollutant removal: a critical review. *Carbon Research,* **2**, 14. https://doi.org/10.1007/s44246-023-00045-5
63. Du C., Xu J., Ding G., He D., Zhang H., Qiu W., Li C., Liao G. (2023) Recent advances in LDH/g-C_3N_4 heterojunction photocatalysts for organic pollutant removal. *Nanomaterials,* **13**, 3066. https://doi.org/10.3390/nano13233066
64. Qiu X., Wang R. (2025) Polyoxometalate-based photocatalytic new materials for the treatment of water pollutants: mechanism, advances, and challenges. *Catalysts,* **15**, 613. https://doi.org/10.3390/catal15070613
65. Bognár S., Despotović V., Finčur N., Putnik P., Jovanović D., Hainz K., Šojić Merkulov D. (2025) Waste-derived photocatalysts for light-driven water treatment: a comprehensive review of green materials from agri-food, industrial, and e-waste. *Separations,* **12**, 337. https://doi.org/10.3390/separations12120337
66. Bissenova M., Idrissov N., Kuspanov Z., Umirzakov A., Daulbayev C., et al. (2025) Hybrid adsorption–photocatalysis composites: a sustainable route for efficient water purification. *Mat. Ren. Sus. Ener.,* **14**, 44. https://doi.org/10.1007/s40243-025-00319-5
67. Bashar M.A., Ibrahim A.B.M., Hasan M.K., Hossain M.S. (2025) Bio-dye-sensitized TiO_2 nanophotocatalysts for visible-light-driven sustainable wastewater treatment. RSC Advances, **15**, 41710–41723. https://doi.org/10.1039/D5RA06120B